Energy Storage Materials 63 (2023) 102956

Contents lists available at ScienceDirect

Energy Storage Materials

journal homepage: www.elsevier.com/locate/ensm

Influence of alkali metal ions (Li^+, Na^+, and K^+) on the redox thermodynamics and kinetics of organic electrode materials for rechargeable batteries

Junxiao Wang, Gaofeng Li, Qi Wang, Liang Huang, Xiaotang Gan, Minle Li, Zhiping Song *

Hubei Key Lab of Electrochemical Power Sources, College of Chemistry and Molecular Sciences, Wuhan University, Wuhan 430072, China

ARTICLE INFO

Keywords:
Organic electrode materials
Alkali metal ions
Thermodynamics
Kinetics
Dual-ion batteries

ABSTRACT

Organic electrode materials have been widely applied in rechargeable Li, Na, and K batteries. However, one of the key scientific issues—the influence of Li^+, Na^+, and K^+ ions on the redox thermodynamics and kinetics is still unclear. Herein, by using n-type poly(anthraquinonyl sulfide) (PAQS) and polyimide (PI) and p-type polytriphenylamine (PTPAn) as examples, we have systematically and deeply studied this problem though elaborate electrochemical tests and theoretical calculations. By employing three-electrode cells, the thermodynamic potentials of Li, Na, K metal electrodes as well as the PAQS, PI, and PTPAn organic electrodes have been accurately measured. They follow the order of $Li^+ > Na^+ > K^+$ for PAQS and PI, and keep unchanged for PTPAn. As an application of this discovery, PAQS–PTPAn dual-ion full-cells show the highest output voltage and low-temperature performance with K^+ ion. To explain the tendency, universal thermodynamic models have been established and the theoretical calculations reveal that with the increase of ionic radius, the interactions of metal ion with electrolyte solvent and discharged n-type organic (N^-) become weaker, which lower down the thermodynamic potential and enhance the redox kinetics. This work provides a significant guidance for the design of high-performance organic batteries.

1. Introduction

Among today's energy storage systems, the development of conventional Li-ion batteries has been limited by theoretical energy densities, safety issues, scarce transition metal (Co, Ni) and Li resources, and environmental concerns [1–3]. In this context, sustainable and environmentally friendly organic electrode materials (OEMs) have received increasing attentions for their enormous potentials in structure design, performance improvement, and application extension [4,5]. Compared with the inorganic counterparts, a significant advantage of OEMs is that the same active material can be applied in many different battery systems because that the electroactive groups in small-molecule organics or amorphous polymers have a wide compatibility with different counterions. For example, as one of the most famous n-type polymer electrode materials, poly(anthraquinonyl sulfide) (PAQS) has been proved applicable with not only Li^+ ion, but also Na^+, K^+, Mg^{2+} ions and even organic cations in nonaqueous electrolytes [6–8].

The great advantages of Na and K in resource abundance and cost as well as the similarities in working principle and cell fabrication have encouraged the shift of research attention from Li-based battery systems to Na- and K-based ones. Especially, the combination of OEMs and Na- or K-based anodes and/or electrolytes is an attractive choice for battery technologies to get rid of the dependence on scarce metals including Li, which is desired for the sustainable development of large-scale energy storage. In the past decade, researchers have devoted enormous effort to extend the application of OEMs from Li batteries to Na and K batteries, and improve their electrochemical performance by molecular design, electrode engineering, and electrolyte optimization [9,10]. However, one of the most important scientific issues—the influence of alkali metal ions (Li^+, Na^+, and K^+) on the redox thermodynamics and kinetics of OEMs, has been neglected or fuzzily understood. On one hand, although the electrochemical performance of many OEMs in different alkali metal battery systems have been reported, there lacks systematic study and strict single-factor comparison to distinguish the effect of alkali metal ions. On the other hand, it is difficult to accurately measure the small potential differences of the organic electrode in different electrolytes through common electrochemical methods, due to the lack of appropriate reference electrodes.

* Corresponding author.
E-mail address: zpsong@whu.edu.cn (Z. Song).

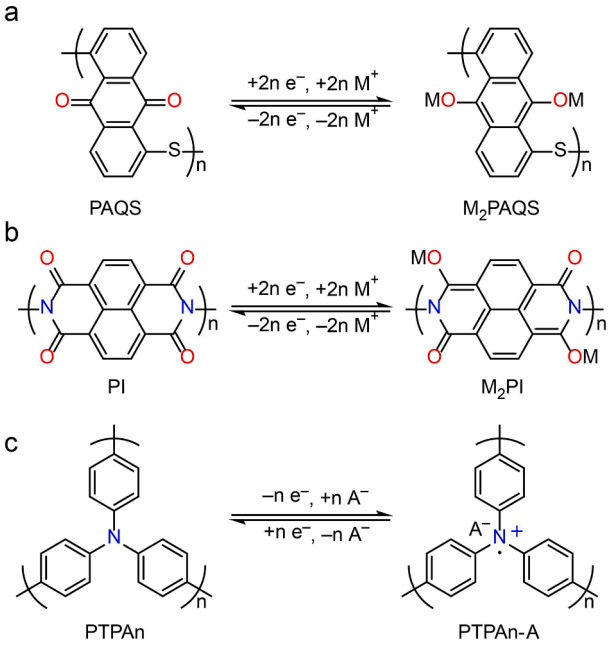
https://doi.org/10.1016/j.ensm.2023.102956
Received 21 July 2023; Received in revised form 4 September 2023; Accepted 5 September 2023
Available online 6 September 2023
2405-8297/© 2023 Elsevier B.V. All rights reserved.

Herein, we take the courage to solve this key scientific problem of OEMs by elaborate electrochemical experiments and theoretical calculations. To avoid the dissolution issue of small-molecular OEMs, we chose three representative polymeric OEMs as examples for studying, including n-type PAQS and polyimide [PI, specifically referring to the one based on 1,4,5,8-naphthalenetetracarboxylic dianhydride (NTCDA) and hydrazine in this work] [11], as well as p-type polytriphenylamine (PTPAn) [12] (Scheme 1). Firstly, we determined the equilibrium potentials of Li, Na, and K metal electrodes in the selected nonaqueous electrolytes for accurate measurements of the charge/discharge potentials of the organic electrodes. Secondly, we figured out the influence laws of Li^+, Na^+, and K^+ ions on the redox thermodynamics and kinetics of n-type and p-type OEMs. Thirdly, as an application of these laws, we assembled PAQS–PTPAn dual-ion full-cells and verified that they can achieve the highest working voltage and low-temperature performance with the electrolyte based on K^+ ion. Finally, by using density functional theory (DFT) calculations, we established universal thermodynamic models and equations to explain the influence laws. To sum up, the research methods and conclusions in this work have a crucial guiding significance in designing rechargeable batteries based on OEMs.

2. Results and discussion

The three representative polymers, PAQS, PI, and PTPAn (Scheme 1), were facilely synthesized according to the previously reported reaction routes illustrated in Fig. S1 [11,13,14]. Their chemical structures were confirmed by Fourier transform infrared (FTIR) spectra (Fig. S2), in which all the characteristic peaks are almost the same as the literature values (Table S1). Scheme 1 presents their electrochemical redox mechanisms, including the n-type reactions of conjugated carbonyl groups (C=O) for PAQS and PI, and the p-type reaction of conjugated N atoms for PTPAn, with alkali metal ions (M^+) and anions (A^-) as the embedded counterions, respectively. According to these redox reactions, the theoretical capacities of PAQS, PI, and PTPAn are 225, 203, and 111 mAh g^{-1}, respectively. The three polymers were made into organic electrodes with the same composition of AM/KB/PTFE = 6:3:1 (AM = active material, KB = Ketjenblack, PTFE = polytetrafluoroethylene) for the following electrochemical tests.

For strict single-factor comparison, it is necessary to choose a series



Scheme 1. Electrochemical redox reactions of (a) PAQS, (b) PI, and (c) PTPAn.

of nonaqueous electrolytes with the same solvent and anion but different M^+ cations. After comprehensive consideration of the material availability, solubility, and electrochemical compatibility, we finally chose 1 M MTFSI/DME [M = Li, Na, and K; TFSI = bis(trifluoromethanesulfonyl) imide; DME = 1,2-dimethoxyethane] solutions as the electrolytes. To accurately measure the electrode potentials during charge/discharge process in the three different electrolytes, it is necessary to employ a universal reference electrode (RE) or different REs with known equilibrium potentials. Unfortunately, as far as we know, there is no such a universal RE that has a constant equilibrium potential and required durability in these different electrolytes. In previous studies [15], the electrode potentials in rechargeable Li, Na, and K batteries have been mostly evaluated using two-electrode coin cells with the alkali metal as both RE and counter electrode (CE). However, it is not applicable to evaluate the small potential differences of the same organic electrode in the different electrolytes. On one hand, the different potential polarizations of Li, Na, and K metal electrodes during charge/discharge process cannot be ignored, so three-electrode cells are more appropriate for the measurements. On the other hand, the relative equilibrium potentials of Li, Na, and K electrodes need be carefully determined. Although the potential values from "Tables of Standard Electrode Potentials" [16], i.e., E_{Li} = –3.04 V, E_{Na} = –2.71 V, and E_K = –2.94 V vs. SHE, have been widely used to calculate their relative potentials (E_{Na} = 0.33 V vs. E_{Li}, E_K = 0.10 V vs. E_{Li}), it may cause significant errors because those values are based on aqueous solution and probably incorrect for nonaqueous electrolytes due to the remarkable effect of M^+ ion solvation [17]. Actually, if following the reactivity trends of the alkali metals, the order should be $E_K < E_{Na} < E_{Li}$, but the exceptionally strong solvation effect of Li^+ ion with water molecules (due to its small radius) greatly lower down E_{Li} to below E_K. To measure the actual equilibrium potentials of M electrode in 1 M MTFSI/DME electrolyte, we designed a two-electrode vial cell using a self-prepared Ag^+/Ag quasi-reference electrode with the mixture of 10 vol% 0.1 M $AgNO_3$/ACN (ACN = acetonitrile) solution and 90 vol% 1 M MTFSI/DME solution as the internal electrolytes (Fig. 1a) [18]. This design can maximally reduce the concentration difference of solvents (ACN and DME) and solutes ($AgNO_3$ and MTFSI) between the internal and external electrolytes and thus the species exchange (which is still considerable in long-time test, and thereby this Ag^+/Ag RE is unapplicable in the subsequent charge–discharge tests). The open-circuit potential curves (Fig. 1c) show that Li and K electrodes have almost the same potential (E_K = –0.01 V vs. E_{Li}), and Na electrode has a 0.20 V higher potential (E_{Na} = 0.20 V vs. E_{Li}).

After determining the relative potentials of Li, Na, and K electrodes, it is possible to measure and compare the charge/discharge potentials of the three organic electrodes by using three-electrode vial cells with them as working electrode (WE) and alkali metals (M = Li, Na, and K) as both RE and CE (Fig. 1b). In the commonly used two-electrode coin cells as half-cells, only one M electrode plays the roles of both RE and CE, and the unavoidable electrochemical polarization and side reactions (of electrolyte to form solid electrolyte interface) make its potential deviating from the thermodynamic equilibrium potential (by several mV) and sometimes unstable. This effect is usually negligible when M = Li, but considerable when M = Na and K due to their much severer side reactions. The three-electrode cell design successfully avoids the potential polarization and thereby ensures the accuracy of measured potentials of the organic electrodes. To fully utilize the electrochemical activity of the OEM and avoid side reactions of the electrolyte, the potential windows (vs. M^+/M) were carefully determined for different RE–WE systems (1.4/1.0/1.3–3.4/3.0/3.3 V for Li/Na/K–PAQS, 1.6/1.2/1.4–3.6/3.2/ 3.4 V for Li/Na/K–PI, and 3.0/2.8/3.0–4.2/4.0/4.2 V for Li/Na/K–PTPAn) in the galvanostatic charge–discharge tests (at 100 mA g^{-1}) and cyclic voltammetry (CV) tests (at 0.1 mV s^{-1}).

The charge–discharge curves of PAQS, PI, and PTPAn after a few cycles (Figs. S3 and S4) are selected as representatives (Fig. 1d–f) for comparison, since the potential polarization and Coulombic efficiency reach a relatively stabilized state. The reversible capacities are

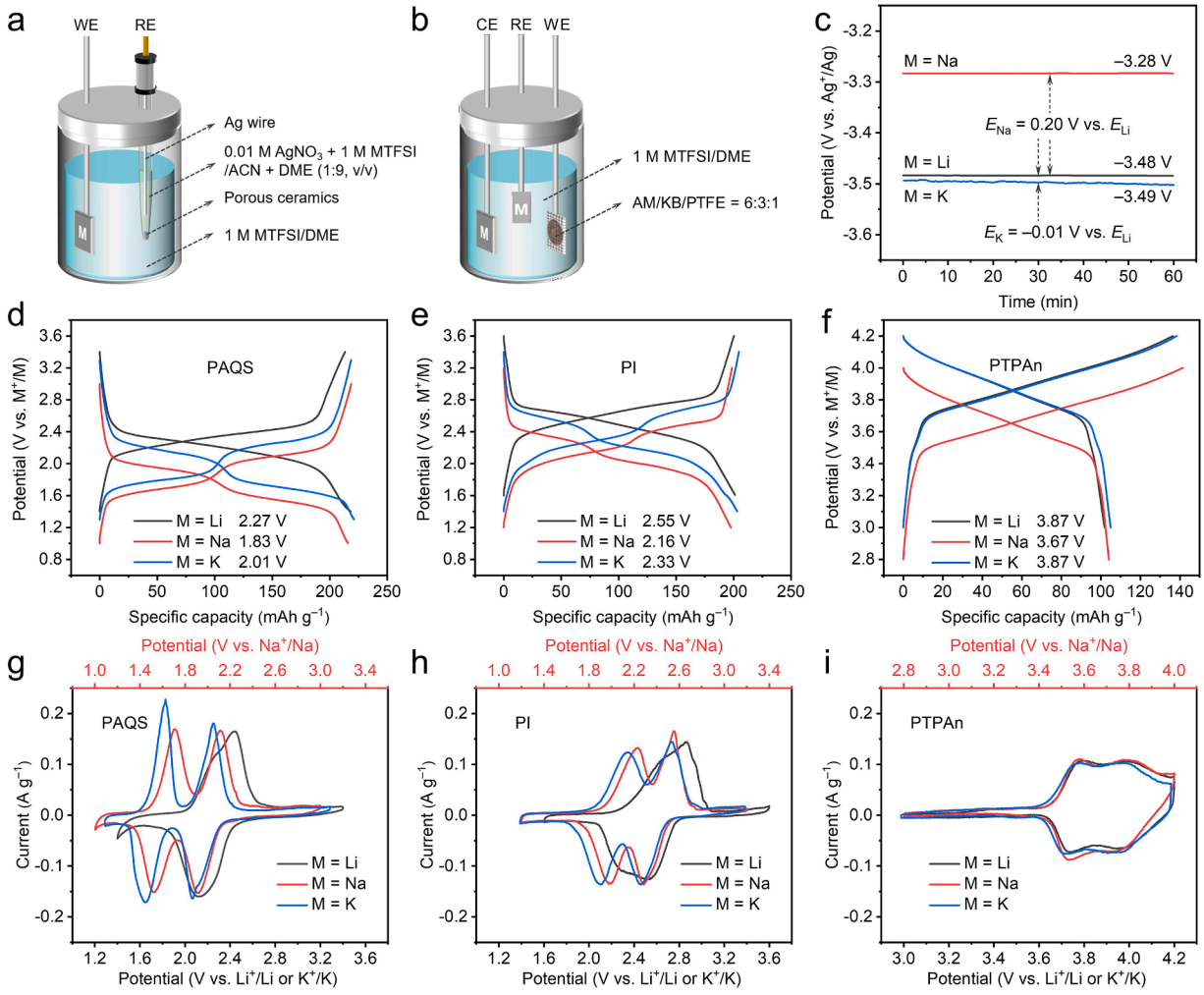


Fig. 1. (a) Schematic of the two-electrode vial cell using an Ag^+/Ag quasi-reference electrode for testing the relative potentials of alkali metal (M = Li, Na, and K) electrodes. (b) Schematic of the three-electrode vial cell using M as both RE and CE for testing the electrochemical performance of the organic (AM = PAQS, PI, and PTPAn) electrodes. (c) Open-circuit potential curves of Li, Na, and K electrodes vs. time measured by the two-electrode vial cell. (d–f) Typical charge–discharge curves at 100 mA g^{-1} (labeled with the corresponding average redox potentials) and (g–i) typical CV curves at 0.1 mV s^{-1} of (d, g) PAQS, (e, h) PI, and (f, i) PTPAn against Li, Na, and K electrodes measured by the three-electrode vial cell (the potentials of CV curves are aligned by using the equations of $E_{Na} = 0.20$ V vs. E_{Li} and $E_K \approx E_{Li}$).

approximately 220, 200, and 110 mAh g^{-1} for PAQS (Fig. 1d), PI (Fig. 1e), and PTPAn (Fig. 1f), respectively, no matter M^+ is Li^+, Na^+, or K^+. They are very close to the theoretical capacities (225, 203, and 111 mAh g^{-1}), indicating that all the three polymers are fully utilized with different M^+ ions. For n-type PAQS and PI, the charge–discharge curves show only one potential plateau when M = Li, but two potential plateaus when M = Na or K, following the output voltage order of Li > K > Na [15]. More quantitatively, Table S2 lists the average charge and discharge potentials, the average of the two that is defined as average redox potential or thermodynamic potential (based on the symmetry of the charge and discharge curves), and the gap of the two that indicates the potential polarization or redox kinetics. The average redox potentials are also listed in Fig. 1d,e, i.e., 2.27/1.83/2.01 V for Li/Na/K–PAQS system, and 2.55/2.16/2.33 V for Li/Na/K–PI system. After aligning the potentials of RE ($E_{Na} = 0.20$ V vs. E_{Li}, $E_K = -0.01$ V vs. E_{Li}), they can be converted to 2.27/2.03/2.00 and 2.55/2.36/2.32 V vs. Li^+/Li for PAQS and PI, respectively. It not only means that PI has a 0.3 V higher redox potential than PAQS, but also indicates that the thermodynamic potentials of inserting Na^+ and K^+ ions are averagely 0.22 and 0.25 V lower than that of inserting Li^+ ion for the two n-type polymers. Besides, the charge–discharge potential gaps (Table S2) follow the order of Li > Na > K for either PAQS (0.21, 0.20, and 0.13 V) or PI (0.19, 0.17, and 0.15 V), suggesting that the redox kinetics can be improved with increase of the alkali metal ion radius. For p-type PTPAn, only a sloping plateau was observed, and the average redox potential is 3.87/3.67/3.87 V against Li/Na/K RE, or 3.87/3.87/3.86 V vs. Li^+/Li, while the charge–discharge potential gap is 0.05/0.05/0.04 V (Table S2). It means that the redox thermodynamics and kinetics of PTPAn are not affected by the kind of M^+ ion, which is reasonable because that it does not participate in p-type reactions. It is worth noting that, the stabilized Coulombic efficiency of Li/Na/K–PTPAn system (about 75%) is much lower than 100% due to the unavoidable oxidation decomposition of the electrolyte in the charge process and the large amount of electrolyte in the three-electrode vial cell. However, it has negligible effect on the above analysis and can be significantly improved by using coin cell containing much less electrolyte (Fig. S4d).

The CV measurements further confirm the above conclusions. For direct comparison of the redox potentials, the original potentials of representative CV curves are aligned by using the equation of $E_{Na} = 0.20$ V vs. E_{Li} and neglecting the 0.01 V gap between E_K and E_{Li} for simplicity (Fig. 1g–i). Apparently, PAQS (Fig. 1g) and PI (Fig. 1h) show only one pair of redox peaks when M = Li. However, the peak shape implies that they are formed by the overlap of two pairs of redox peaks with close potentials. When M = Na and K, the peaks are split to be distinguishable

and shift towards lower potentials with increase of the alkali metal ion radius. For PTPAn (Fig. 1i), as expected, the CV curves show negligible difference for different M^+ ions.

Obviously, the declining trend of the redox potentials of n-type OEMs with Li^+, Na^+, and K^+ ions will reduce the output voltages of Na–organic and K–organic batteries compared to that of Li–organic battery. After taking the relative potentials of alkali metal anodes into account, roughly, it is reduced by 0.4 V for Na–organic battery or 0.2 V for K–organic battery, which is remarkable if considering the difficulty of elevating redox potential by molecular design. This drawback counteracts the advantages of Na and K in resource sustainability and cost to some extent. However, it can be also regarded as an advantage for dual-ion batteries using n-type OEMs as anodes to match with p-type cathodes including OEMs and graphite, because lower anode potential leads to higher output voltage of the full-cell. Especially, because that M^+ ions have no effect on the redox potential of p-type OEM, it is expected that the dual-ion battery composed of n-type organic anode and p-type organic cathode will follow the order of output voltages of $Li^+ < Na^+ < K^+$.

To verify the above hypothesis, we assembled all-organic dual-ion full-cells by using PAQS or PI as anode, PTPAn as cathode, and 1 M MTFSI/DME solution as electrolyte, as shown in Fig. 2a. The operation of the cell stats with a charge process, in which the p-type cathode is oxidized and accompanied by the embedding of $TFSI^-$ anions, while the n-type anode is reduced and accompanied by the insertion of M^+ cations. In the reverse discharge process, the anions and cations are extracted from the electrodes and move back to the electrolyte. Fig. 2b summarizes the thermodynamic potentials of the PAQS, PI, and PTPAn electrodes against M electrode in 1 M MTFSI/DME electrolyte (M = Li, Na, and K). Based on these data the thermodynamic voltages of the PAQS–PTPAn and PI–PTPAn full-cells are predicted to be 1.60/1.84/1.86 V and 1.32/1.51/1.54 V when M = Li/Na/K, respectively.

All the six full-cells realize reversible capacities close to the theoretical value (111 mAh g^{-1} based on the PTPAn cathode) and stable cycling of 100 cycles at room temperature (Fig. S5a,b). The representative charge–discharge curves are shown in Fig. 2c,d. The average redox voltages are 1.63/1.76/1.81 V and 1.32/1.42/1.46 V for PAQS–PTPAn and PI–PTPAn systems when M = Li/Na/K, with the same order as predicted. The practical voltages are almost equal to the predicted ones when M = Li, and slightly lower (by 0.05–0.09 V) than those when M = Na and K. It is reasonable because that the N/P capacity ratio was set to 1.25, and thus the incomplete utilization of PAQS or PI anode slightly reduced the output voltage, but the influence is more remarkable when M = Na and K due to the much wider redox potential range of

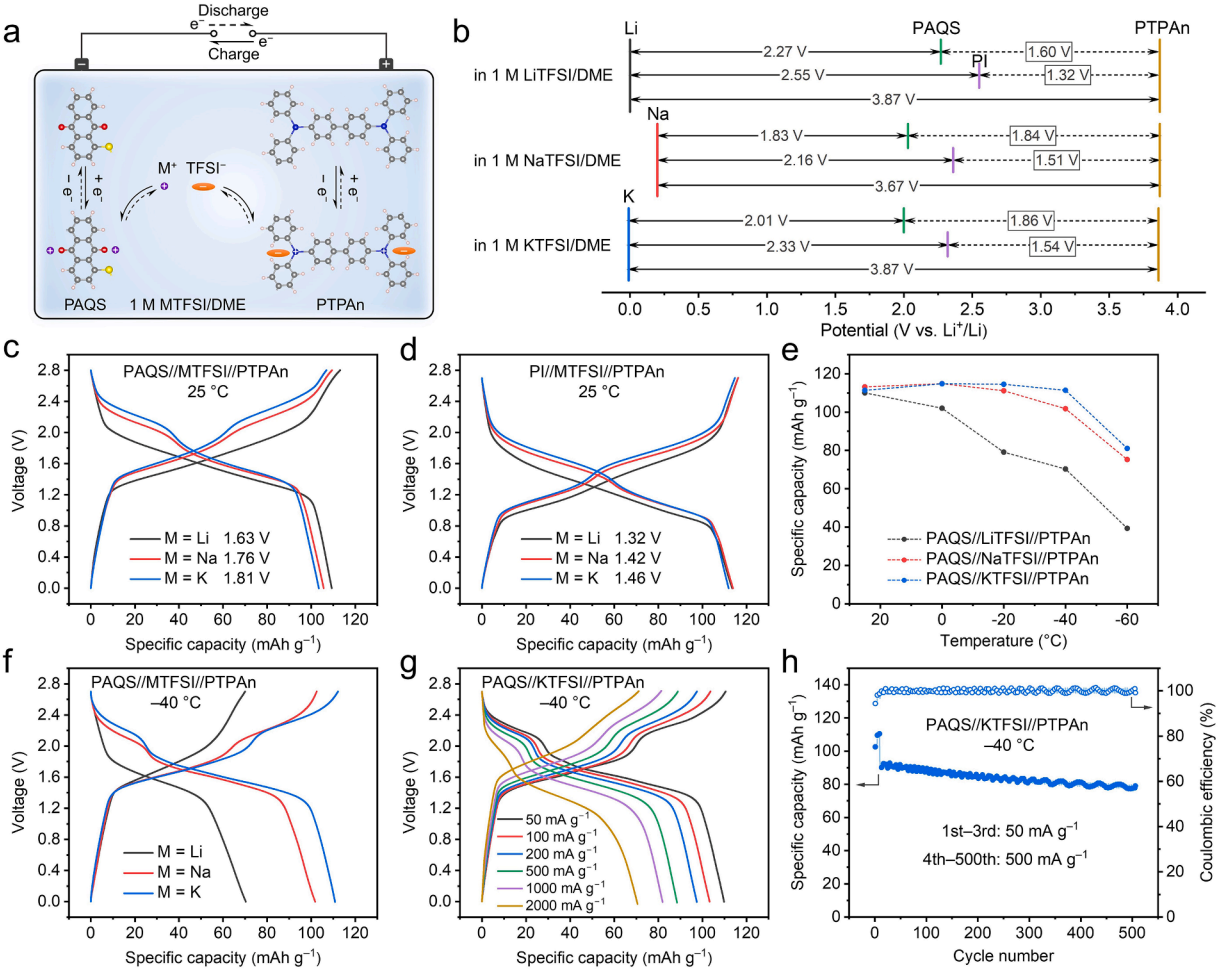


Fig. 2. (a) Schematic of the all-organic dual-ion full-cell based on PAQS anode, PTPAn cathode, and 1 M MTFSI/DME (M = Li, Na, and K) electrolyte. (b) Comparison of the thermodynamic redox potentials of the PAQS, PI, and PTPAn electrodes, and predicted output voltages of the PAQS–PTPAn and PI–PTPAn full-cells using different electrolytes. (c, d) Typical charge–discharge curves of the (c) PAQS//MTFSI//PTPAn and (d) PI//MTFSI//PTPAn cells at 25 °C (labeled with the corresponding average redox voltages). (e) Reversible capacities at different temperatures (25, 0, –20, –40, and –60 °C) and (f) typical charge–discharge curves at –40 °C of the PAQS//MTFSI//PTPAn cells. (g) Typical charge–discharge curves under different current rates (50, 100, 200, 500, 1000, and 2000 mA g^{-1}) and (h) long-term cycling performance of the PAQS//KTFSI//PTPAn cell at –40 °C. The specific capacities and current rates (100 mA g^{-1} unless otherwise specified) are based on the mass of PTPAn in the cathode.

anode (Fig. 1d,e). Anyway, the above results prove that replacing Li^+ ion with Na^+ or K^+ ion is an efficient approach to increase the output voltage of an all-organic dual-ion full-cell by 0.1–0.2 V, in addition to the advantages of much lower cost and higher sustainability.

Besides lower thermodynamic potential, it is also speculated that larger M^+ ion can bring about faster redox kinetics for PAQS and PI [15], as implied by the smaller charge–discharge potential gap (Table S2). Since both PAQS and PI have intrinsically fast redox kinetics because of their pseudocapacitive character, it is difficult to evaluate the difference among the kinetics with different M^+ ions by commonly used rate performance tests at room temperature. Considering that the redox kinetics is sensitive to temperature, we compared the charge–discharge performance of the PAQS–PTPAn full-cells (which were chosen because of higher output voltage and energy density than the PI–PTPAn system) at lower testing temperatures of 0, –20, –40, and –60 °C (Fig. S5c–f). The ionic conductivities of the 1 M MTFSI/DME electrolytes at these temperatures were previously measured to assess the feasibility. As shown in Fig. S6, whatever M is, they possess almost the same ionic conductivity at each temperature and follow a slow decreasing tendency with temperature decline, except for that there is a sudden drop for 1 M MTFSI/DME electrolyte at –40 and –60 °C. It is probably caused by the partial precipitation of LiTFSI (Fig. S7), which has smaller solubility than NaTFSI and KTFSI due to stronger interaction between Li^+ and $TFSI^-$ ions. Anyway, all the ionic conductivities are still higher than 1 mS cm^{-1} even at –60 °C, indicating that they are unlikely to be the limiting factor of the redox kinetics.

The reversible capacities with different M^+ ions are summarized in Fig. 2e. Obviously, relative to the reversible capacity at 25 °C (~110 mAh g^{-1}), the capacity retention decline with decrease of temperature as well as the alkali metal ion radius. More specifically, compared to Li^+ ion, Na^+ ion provides significantly improved capacity retentions at low temperature (≤ 0 °C), and K^+ ion further shows a slight superiority to Na^+ ion. For instance, at –40 °C, the reversible capacities are 70, 101, and 110 mAh g^{-1} for Li^+, Na^+, and K^+ ion, respectively (Fig. 2f). Since different M^+ ions have no impact on the redox reaction thermodynamics and kinetics of the p-type cathode (PTPAn), the only possible reason is that they cause different potential polarizations of the n-type anode (PAQS). In the charge process of the full-cell, larger polarization will lower down the anode potential and accordingly the charge cutoff potential of cathode, because their potential gap is limited by the given cutoff voltage (2.8 V). Therefore, the charge capacity of cathode that determines the reversible capacity of full-cell is also reduced because of the relation between charge capacity and cutoff potential of PTPAn (Fig. 1f). To give full play of the redox kinetics, we further tested the rate performance at –40 °C (Fig. S8). As expected, the PAQS//KTFSI//PTPAn system shows the highest rate capability, i.e., the capacity retentions relative to that at 50 mA g^{-1} are 94%, 88%, 80%, 75%, and 65% at 100, 200, 500, 1000, and 2000 mA g^{-1}, respectively (Fig. 2g). Furthermore, it also exhibits excellent long-term cycling stability at –40 °C (Fig. 2h). After activation under 50 mA g^{-1} for three cycles, the cell was further cycled under a current rate of 500 mA g^{-1} and achieved a reversible capacity of 92 mAh g^{-1}. The capacity slowly decreases to 79 mAh g^{-1} at the 500th cycle, corresponding to a high retention of 86%. To sum up, among the three M^+ ions, K^+ is the most preferred one for the all-organic dual-ion batteries, which provides not only the highest output voltage, but also the fastest redox kinetics for low-temperature, high-rate, and long-term application.

To uncover the influencing mechanism of the alkali metal ions, we established universal thermodynamic models and cycles for alkali metal (M), n-type organic (N), and p-type organic (P) electrodes (Fig. 3). Generally, the reduction process of a M electrode consists of two steps: desolvation of the M^+ ion in solution phase [$M^+_{(s)}$] to that in gas phase [$M^+_{(g)}$], and further reduction to M atom by receiving one electron, corresponding to Gibbs free energy changes of $-\Delta G_s(M^+)$ and $\Delta G_r(M)$, respectively. According to the thermodynamic cycle (Fig. 3a) [19], the absolute reduction potential of the M electrode (E_M) can be calculated by the below equation [20],

$$E_M = \frac{\Delta G_r(M) - \Delta G_s(M^+)}{-F} = \frac{-\Delta G_{ion}(M) - \Delta G_{sub}(M) - \Delta G_s(M^+)}{-F} \quad (1)$$

where ΔG_{ion} is the free energy of metal ionization in gas phase, ΔG_{sub} is the heat of metal sublimation, and F is the Faraday's constant. Similarly, an N electrode also follows the two steps of desolvation and reduction, resulting in the product of M^+N^- (Fig. 3b). As an approximation, the solvation energies of the electronically neutral species, i.e., N and M^+N^-, are neglected or it can be assumed that they counteract with each other. Then the absolute reduction potential of the N electrode (E_N) can be expressed by the below equation.

$$E_N = \frac{\Delta G_r(N) - \Delta G_s(M^+)}{-F} \quad (2)$$

As for an P electrode, the reduction is accompanied by the release of

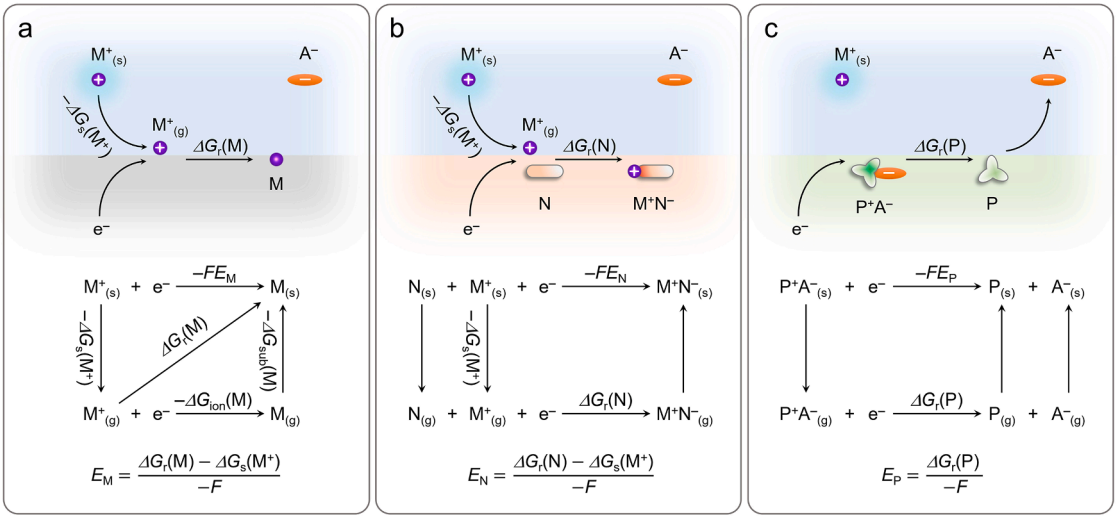


Fig. 3. Schematics of electrochemical reduction processes and thermodynamic cycles for the caculations of theoretical reduction potentials (E) of (a) alkali metal (M), (b) n-type organic (N), and (c) p-type organic (P) electrodes. ΔG_s is the metal ion solvation free energy, ΔG_r is the Gibbs free energy change of reduction process, ΔG_{ion} is the free energy of metal ionization in gas phase, ΔG_{sub} is the heat of metal sublimation [$\Delta G_r(M) = -\Delta G_{ion}(M) - \Delta G_{sub}(M)$], and F is the Faraday's constant. The subscripts, (s) and (g), denote the solution and gas phases, respectively.

anion (A^-) without the participation of M^+ ion (Fig. 3c). Unlike M^+ cation, the solvation energy of A^- anion can be ignored due to the negligible anion-solvent interaction [21]. Similarly, the solvation energies of the electronically neutral P^+A^- and P are also not taken into account, and thus the absolute reduction potential of the P electrode (E_P) is determined by the below equation.

$$E_P = \frac{\Delta G_r(P)}{-F} \tag{3}$$

In this context, the thermodynamic voltages of the M–N half-cell (ΔE_{M-N}), M–P half-cell (ΔE_{M-P}), and N–P full-cell (ΔE_{N-P}) can be calculated by the below equations.

$$\Delta E_{M-N} = E_N - E_M = \frac{\Delta G_r(N) - \Delta G_r(M)}{-F} \tag{4}$$

$$\Delta E_{M-P} = E_P - E_M = \frac{\Delta G_r(P) - \Delta G_r(M) + \Delta G_s(M^+)}{-F} \tag{5}$$

$$\Delta E_{N-P} = E_P - E_N = \frac{\Delta G_r(P) - \Delta G_r(N) + \Delta G_s(M^+)}{-F} \tag{6}$$

For M–N half-cell, the voltage is independent with $\Delta G_s(M^+)$ because that the solvation and desolvation of M^+ ion always occur simultaneously on the M and N electrode and thus the energy changes are counteracted. In contrast, for M–P half-cell and N–P full-cell, only anode (M or N) involves the solvation/desolvation of M^+ ion, so $\Delta G_s(M^+)$ may be a key factor of determining the output voltage. Obviously, $\Delta G_s(M^+)$ is mainly depended on the kinds of solvent and alkali metal ion. In our previous study [18], the strong effect of solvent has been already confirmed. In this work, we will reveal the influence of alkali metal ion.

It is worth noting that, herein the solvation energy, $\Delta G_s(M^+)$, refers to the free energy change of transferring M^+ ion from the hypothetical ideal-gas phase into the electrolyte solution phase, which essentially represents the chemical potential of M^+ ion [17,22]. It is different from the binding process between one M^+ ion and n solvent molecules (e.g., DME) to form a solvation cluster [e.g., $M^+(DME)_n$], for which the free

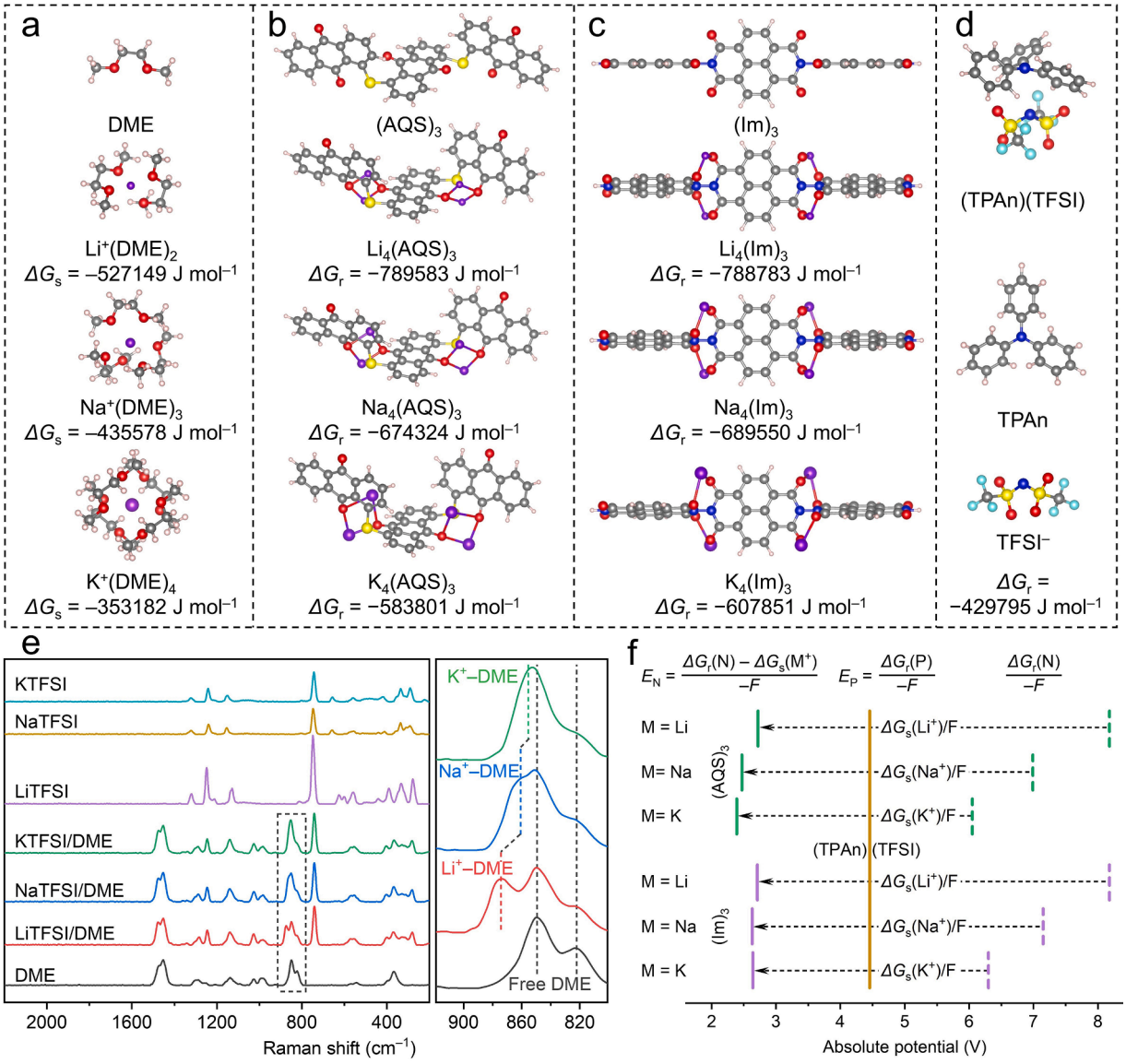


Fig. 4. (a) Solvation structures and solvation energies (ΔG_s) of Li^+, Na^+, and K^+ ions in DME. (b–d) Geometrical configurations (C, gray; H, pink; O, red; N, blue; S, yellow; F, cyan; Li, Na, and K, violet) of (b) $(AQS)_3$, (c) $(Im)_3$, and (d) (TPAn)(TFSI) molecules (as model molecules of PAQS, PI, and PTPAn, respectively) and their discharge products, as well as the calculated Gibbs free energy changes of the reduction reactions (ΔG_r). (e) Raman spectra of 1 M MTFSI/DME (M = Li, Na, and K) electrolytes and the corresponding MTFSI salts and DME solvent. (f) Theoretical reduction potentials of $(AQS)_3$, $(Im)_3$, and (TPAn)(TFSI) molecules in the electrolytes obtained by DFT calculations.

energy change is denoted as ΔG_{bind}. In this study, $\Delta G_s(M^+)$ is calculated by the general cluster–continuum solvation method using Gaussian 16 program [23], and the derivation is detailed in Fig. S9 and Table S3–S5 [24,25]. The $M^+(DME)_n$ clusters are constructed (Fig. 4a) for the calculation of ΔG_{bind}, which is necessary in the derivation of $\Delta G_s(M^+)$ [26]. According to the previous literature [27], the coordination number, n, is determined as 2, 3, and 4 for $M^+ = Li^+$, Na^+, and K^+, respectively. According to Eq. S5, Table S4, and Table S5, the differences among the three $\Delta G_s(M^+)$ values mainly come from the different $\Delta G_{bind(g)}$ (binding energies in gas phase). More specifically, with increase of the ion size of M^+ (from Li^+ to Na^+ and K^+), the M^+–DME interaction becomes weaker, and both $\Delta G_{bind(g)}$ and $\Delta G_s(M^+)$ (listed in Fig. 4a) become smaller (less negative) [28,29]. After figuring out $\Delta G_s(M^+)$, E_M can be easily calculated according to Eq. (1) and Table S6. The results are 1.58, 1.74, and 1.60 V for M = Li, Na, and K, respectively. It is very consistent with the experimental results that Li and K have almost the same thermodynamic potential and Na has a 0.20 V higher one.

To show the different M^+–DME interactions more clearly, we recorded the Raman spectra of the three 1 M MTFSI/DME electrolytes as well as the individual components (Fig. 4e). Compared to the bare DME solvent, a new peak is observed for the three electrolytes at the left of the characteristic peaks of free DME solvent (at 850 and 822 cm^{-1}), owing to the coordination between alkali metal ion and solvent molecules [30]. The peak position is strongly correlated with the kind of M^+ ion, i.e., 874, 860, and 855 cm^{-1} for Li^+, Na^+, and K^+, respectively. The red-shift extent is an effective index to evaluate the interaction strength, which follows the order of Li^+–DME > Na^+–DME > K^+–DME. It is reasonable because of the decreasing of ion charge density and in agreement with the tendency of calculated $\Delta G_{bind(g)}$ and $\Delta G_s(M^+)$ values.

Besides $\Delta G_s(M^+)$, the Gibbs free energy changes of reduction reactions, i.e., $\Delta G_r(M)$, $\Delta G_r(N)$, and $\Delta G_r(P)$ need to be figure out for the calulaitons of ΔE_{M-N}, ΔE_{M-P}, and ΔE_{N-P} [Eqs. (4)–(6)]. In the calculation of E_M, the $\Delta G_r(M)$ values have been already obtained (Table S6). For the calculations of $\Delta G_r(N)$ and $\Delta G_r(P)$, we constructed $(AQS)_3$, $(Im)_3$, and (TPAn)(TFSI) as model molcules to simulate PAQS, PI, and PTPAn in oxidation state, as well as $M_4(AQS)_3$, $M_4(Im)_3$, TPAn, and TFSI to simulate the discharge products (Fig. 4b–d). Their molecular structures, optimized geometrical configurations, and Gibbs free energies are listed in Table S7, and the electrostatic potential maps of the molecules in the pristine state [$(AQS)_3$, $(Im)_3$, and TPAn] are presented in Fig. S10 to indicate the active sites. Table S8 summerizes the reduction reactions and the calculation process of Gibbs free energy changes for per electron, i.e., ΔG_r.

For n-type PAQS and PI, $\Delta G_r(N)$ follows the same tendency as for $\Delta G_r(M)$ and $\Delta G_s(M^+)$, i.e., becoming smaller (less negative) from Li^+ to Na^+ and K^+ ions. It suggests that the decreased charge density of M^+ ion also weakens its interaction with the discharged n-type organic molecule (N^-). Subsequently, according to Eq. (2), the absolute potentials (E_N) are calculated to be 2.72, 2.47, and 2.39 V for PAQS and 2.71, 2.63, and 2.64 V for PI, when M = Li, Na, and K, respectively (Table S9). Approximately, the tendency agrees with the experimental results that Na^+ and K^+ ions bring about similar redox potentials, which are about 0.2 V lower than that with Li^+ ion.

For p-type PTPAn, $\Delta G_r(P)$ is indepentent to M^+ ion, and the absolute potentials (E_P) is calculated to be constantly 4.45 V no matter the cation is Li^+, Na^+, or K^+ (Table S8 and Table S9). According to Eq. S11, i.e., $\Delta E_{N-P} = E_P - E_N$, the theoretical output voltages of full-cells are calculated to be 1.73, 1.98, and 2.06 V for the PAQS–PTPAn system, and 1.74, 1.82, and 1.81 V for the PI–PTPAn system when $M^+ = Li^+$, Na^+, and K^+. Although these values are 0.1–0.4 V higher than the experimental data (Fig. 2c,d), it clearly verify the output voltage order of $Li^+ < Na^+ < K^+$.

Fig. 4f summarizes all the calculated absolute potentials of PAQS, PI, and PTPAn with different M^+ ions. If ignoring the solvation energy, $\Delta G_s(M^+)$, the potential of n-type organic in gas phase is equal to $-\Delta G_r(N)/F$, which is much higher than $E_P = -\Delta G_r(P)/F$ and shows huge differences among Li^+, Na^+, and K^+ ions. The introduction of $\Delta G_s(M^+)$ greatly lowers down the absolute potentials of n-type organics $\{E_N = [\Delta G_r(N) - \Delta G_s(M^+)]/(-F)\}$ to below E_P and narrows the gaps among Li^+, Na^+, and K^+ ions. To sum up, as the ionic radius increases and the charge density decreases from Li^+ ion to Na^+ and K^+ ions, their interactions with both the electrolyte solvent and the discharged n-type organic (N^-) become weaker, causing large reduction of $\Delta G_s(M^+)$ and $\Delta G_r(N)$, respetively, and finally slight reduction of E_N.

To evaluate the influence of different M^+ ions on the redox kinetics of n-type PAQS and PI, we measured the O···M bond lengths in the optimized geometrical configurations of $M_4(AQS)_3$ and $M_4(Im)_3$ molecules (Fig. 4b, c). Table S9 lists the average bond lengths, which are 1.83, 2.21, and 2.60 Å for the $(AQS)_3$ series, as well as 1.81, 2.18, and 2.55 Å for the $(Im)_3$ series when M = Li, Na, and K. They follow the same order as the $M^+(DME)_n$ clusters (1.92, 2.34, and 2.73 Å) and reflect the weakening of interactions between M^+ and N^-, which is beneficial to the redox kinetics of n-type organic electrode materials.

3. Conclusion

In summary, for the first time we systematically and deeply studied the influence of alkali metal ions ($M^+ = Li^+$, Na^+, and K^+) on the redox thermodynamics and kinetics of organic electrode materials. Three polymer electrode materials including n-type PAQS and PI as well as p-type PTPAn were chosen as representatives, and 1 M MTFSI/DME solutions were employed as electrolytes. Firstly, the relative equilibrium potentials of the alkali metal electrodes are determined to be $E_{Na} = 0.20$ V vs. E_{Li} and $E_K = -0.01$ V vs. E_{Li}. On this basis, the thermodynamic potentials of the three polymers have been accurately evaluated by using three-electrode cells. They follow the order of $Li^+ > Na^+ > K^+$ for PAQS and PI, and keep unchanged for PTPAn. As an application of these findings, PAQS–PTPAn dual-ion full-cells have been assembled and show the highest output voltage as well as low-temperature performance with K^+ ion. Finally, we established universal thermodynamic models and equations to calculate the thermodynamic potentials of alkali metals, n-type organics, and p-type organics. The results show high consistence with the experimental results and prove that the largest K^+ ion possesses the weakest interactions with both the electrolyte solvent and the discharged n-type organic (N^-), and thus the lowest thermodynamic potential and the fastest redox kinetics. This work provides fundamental new knowledge about organic electrode materials, which are crucial for the scientific design of organic batteries.

4. Experimental section

4.1. Material synthesis

Poly(anthraquinonyl sulfide) (PAQS), polyimide (PI), and polytriphenylamine (PTPAn) were synthesized by reference to the previous reports [11,13,14]. Their synthesis routes are presented in Fig. S1. All the raw materials and solvents were purchased from Adamas and used without further purification.

PAQS was synthesized by a condensation polymerization of 1,5-dichloroanthraquinone (DCAQ) monomer [13]. Firstly, 2.77 g (0.01 mol) of DCAQ was dissolved in 50 mL of 1-methyl-2-pyrrolidone (NMP) and 0.46 g (0.01 mol) of anhydrous Li_2S was added into the solution. The mixture was refluxed (at 205 °C) under stirring for 6 h in nitrogen atmosphere. After cooling to room temperature, the solid was collected and washed successively with NMP and acetone. The product was dried at 80 °C in air, and PAQS was obtained as a brown powder with a yield of 89%.

PI was synthesized by a two-step condensation polymerization of 1,4,5,8-naphthalenetetracarboxylic dianhydride (NTCDA) monomer [11]. Firstly, 2.68 g (0.01 mol) of NTCDA and 1.30 mL (0.022 mol) of hydrazine hydrate (85%) were added into 80 mL of ethanol, and the mixture was refluxed (at 78 °C) under stirring for 6 h. The solid was collected by hot filtration and washed with ethanol subsequently. The

product was dried at 80 °C in vacuum for 12 h, and 1,4,5,8-N,N'-diaminonaphthalenecarboximide (DANTCBI) was obtained as a yellow powder with a yield of 87%. Secondly, 1.48 g (0.005 mol) of DANTCBI and 1.34 g (0.005 mol) of NTCDA were added into 40 mL of *p*-chlorophenol, and the mixture was refluxed (at 220 °C) under stirring for 8 h in nitrogen atmosphere. After cooling to room temperature, the solid was collected and washed successively with NMP and acetone. The product was further heated at 350 °C for 8 h in nitrogen atmosphere, and PI was obtained as a dark yellow powder with a yield of 51%.

PTPAn was synthesized by an oxidation polymerization of triphenylamine (TPAn) monomer [14]. Firstly, 2.45 g (0.01 mol) of TPAn was dissolved in 40 mL of $CHCl_3$ under stirring, and 6.49 g (0.04 mol) of anhydrous $FeCl_3$ as oxidant was added into the solution in batches during 3 h. The mixture was further stirred at room temperature for 2 h in nitrogen atmosphere, and then poured into 60 mL of methanol to precipitate the polymer. For further purification, the collected solid was dissolved again in $CHCl_3$, and the insoluble residues were removed by filtration. The product was precipitated by adding methanol, washed with it several times, dried at 60 °C in vacuum for 12 h, and finally PTPAn was obtained as a white powder with a yield of 76%.

4.2. Characterization methods

The structures of the synthesized polymers were confirmed by Fourier transform infrared (FTIR) spectroscopy using KBr pellets, which were conducted on an ALPHA II spectrometer (Bruker, Germany) in the wavenumber range of 400–4000 cm^{-1}. The electrolyte salts, solvent, and solutions were characterized by Raman spectroscopy conducted on an ATP3200 spectrometer (Optosky, Xiamen, China) using a 785 nm laser. The ionic conductivities of the electrolytes at different temperatures were tested by using a DDB-303A conductivity meter (INESA, China).

4.3. Electrochemical tests

A typical rolling method was employed to fabricate the organic electrodes. The active material (PAQS, PI, and PTPAn) was mixed with Ketjenblack (KB, EC-600JD) conductive carbon and polytetrafluoroethylene (PTFE) binder in a weight ratio of 6:3:1, and the homogeneous mixture was rolled into a thin film. It was then dried in air at 60 °C and cut into 8 mm-diameter disks, which were pressed onto aluminum mesh current collectors. The mass loading of active material was controlled at ~1.5 mg cm^{-2} for PAQS or PI and ~2.5 mg cm^{-2} for PTPAn. The electrolytes were simply prepared by dissolving bis(trifluoromethanesulfonyl)imide salts of lithium, sodium, and potassium (MTFSI, M = Li, Na, and K) into 1,2-dimethoxyethane (DME) solvent with a concentration of 1 M.

Two-electrode and three-electrode vial cells as illustrated in Fig. 1a and b were prepared in a glovebox filled with argon. The nonaqueous Ag^+/Ag quasi-reference electrode (RE) was fabricated by immersing an Ag wire in the self-prepared electrolyte composed of 10 vol% 0.1 M $AgNO_3$/acetonitrile solution and 90 vol% 1 M MTFSI/DME solution. Alkali metal (M) electrodes and organic electrodes were attached to stainless steel wires.

CR2025-type coin cells were also assembled in the glovebox filled with argon, by matching PAQS or PI anode (N) with PTPAn cathode (P) in a N/P capacity ratio of 1.25. A glass fiber membrane (GF/A, Whatman) was sandwiched between two Celgard 2325 membranes to act as a separator, which was soaked by about 100 μL of 1 M MTFSI/DME electrolyte. Coin cells consisting of PTPAn cathode and excessive Li metal anode were also similarly fabricated for comparison with the three-electrode cells.

The two-electrode vial cells were used to test the open-circuit potentials vs. time on a PRATAT MC electrochemical station (Princeton Applied Research, USA). The three-electrode vial cells (half-cells) and coin cells (full-cells) were used to test the galvanostatic charge–discharge performance on a CT-4008T battery test system (Neware, Shenzhen, China). The current rate was fixed at 100 mA g^{-1} based on the active material weight of working electrode (WE) or cathode, unless otherwise stated. The three-electrode cells were also tested by cyclic voltammetry (CV) method at a scan rate of 0.1 mV s^{-1}, on the electrochemical station. Most of the electrochemical tests were performed at 25 °C, and lower temperatures of 0, –20, –40, and –60 °C were also used for charge–discharge tests of full-cells.

4.4. DFT calculations

All DFT calculations were carried out using Gaussian 16 program [23]. Geometry optimization and frequency analysis of organic molecules were performed at B3LYP/6-31+G(d, p) level and solvation Gibbs free energies (ΔG_s) of Li^+, Na^+, and K^+ ions were calculated at M06-2X/6-31+G(d) level.

CRediT authorship contribution statement

Junxiao Wang: Methodology, Investigation, Data curation, Visualization, Formal analysis, Investigation, Writing – original draft, Writing – review & editing. **Gaofeng Li:** Methodology. **Qi Wang:** Investigation. **Liang Huang:** Investigation. **Xiaotang Gan:** Investigation. **Minle Li:** Investigation. **Zhiping Song:** Conceptualization, Methodology, Funding acquisition, Project administration, Supervision, Writing – review & editing.

Declaration of Competing Interest

The authors declare that they have no known competing financial interests or personal relationships that could have appeared to influence the work reported in this paper.

Acknowledgments

The authors gratefully acknowledge financial support from the National Key Research and Development Program of China (2022YFB2402201), the National Natural Science Foundation of China (Nos. 21975189 and 22179102), and the Recruitment Program for Young Professionals. The authors also acknowledge the Supercomputing Center of Wuhan University for supercomputing system.

Supplementary materials

Supplementary material associated with this article can be found, in the online version, at doi:10.1016/j.ensm.2023.102956.

References

[1] M. Li, J. Lu, Z. Chen, K. Amine, 30 years of lithium-ion batteries, Adv. Mater. 30 (2018), 1800561, https://doi.org/10.1002/adma.201800561.
[2] N.A. Kyeremateng, R. Hahn, Attainable energy density of microbatteries, ACS Energy Lett. 3 (2018) 1172–1175, https://doi.org/10.1021/acsenergylett.8b00500.
[3] Y. Tian, G. Zeng, A. Rutt, T. Shi, H. Kim, J. Wang, J. Koettgen, Y. Sun, B. Ouyang, T. Chen, Z. Lun, Z. Rong, K. Persson, G. Ceder, Promises and challenges of next-generation "beyond li-ion" batteries for electric vehicles and grid decarbonization, Chem. Rev. 121 (2021) 1623–1669, https://doi.org/10.1021/acs.chemrev.0c00767.
[4] T.B. Schon, B.T. McAllister, P.F. Li, D.S. Seferos, The rise of organic electrode materials for energy storage, Chem. Soc. Rev. 45 (2016) 6345–6404, https://doi.org/10.1039/c6cs00173d.
[5] P. Poizot, J. Gaubicher, S. Renault, L. Dubois, Y. Liang, Y. Yao, Opportunities and challenges for organic electrodes in electrochemical energy storage, Chem. Rev. 120 (2020) 6490–6557, https://doi.org/10.1021/acs.chemrev.9b00482.
[6] Y. Zhang, Y. Huang, G. Yang, F. Bu, K. Li, I. Shakir, Y. Xu, Dispersion-assembly approach to synthesize three-dimensional graphene/polymer composite aerogel as a powerful organic cathode for rechargeable Li and Na batteries, ACS Appl. Mater. Interfaces 9 (2017) 15549–15556, https://doi.org/10.1021/acsami.7b03687.
[7] Z. Jian, Y. Liang, I.A. Rodríguez-Pérez, Y. Yao, X. Ji, Poly(anthraquinonyl sulfide) cathode for potassium-ion batteries, Electrochem. Commun. 71 (2016) 5–8, https://doi.org/10.1016/j.elecom.2016.07.011.

[8] J. Bitenc, K. Pirnat, T. Bančič, M. Gaberšček, B. Genorio, A. Randon-Vitanova, R. Dominko, Anthraquinone-based polymer as cathode in rechargeable magnesium batteries, ChemSusChem 8 (2015) 4128–4132, https://doi.org/10.1002/cssc.201500910.
[9] X. Yin, S. Sarkar, S. Shi, Q.A. Huang, H. Zhao, L. Yan, Y. Zhao, J. Zhang, Recent progress in advanced organic electrode materials for sodium-ion batteries: synthesis, mechanisms, challenges and perspectives, Adv. Funct. Mater. 30 (2020), 1908445, https://doi.org/10.1002/adfm.201908445.
[10] W. Zhang, W. Huang, Q. Zhang, Organic materials as electrodes in potassium-ion batteries, Chem. Eur. J. 27 (2021) 6131–6144, https://doi.org/10.1002/chem.202005259.
[11] Z. Song, H. Zhan, Y. Zhou, Polyimides: promising energy-storage materials, Angew. Chem. Int. Ed. 49 (2010) 8444–8448, https://doi.org/10.1002/anie.201002439.
[12] J.K. Feng, Y.L. Cao, X.P. Ai, H.X. Yang, Polytriphenylamine: a high power and high capacity cathode material for rechargeable lithium batteries, J. Power Sources 177 (2008) 199–204, https://doi.org/10.1016/j.jpowsour.2007.10.086.
[13] Z. Song, H. Zhan, Y. Zhou, Anthraquinone based polymer as high performance cathode material for rechargeable lithium batteries, Chem. Commun. 4 (2009) 448–450, https://doi.org/10.1039/b814515f.
[14] W. Deng, X. Liang, X. Wu, J. Qian, Y. Cao, X. Ai, J. Feng, H. Yang, A low cost, all-organic Na-ion battery based on polymeric cathode and anode, Sci. Rep. 3 (2013) 2671, https://doi.org/10.1038/srep02671.
[15] Y. Hu, Y. Gao, L. Fan, Y. Zhang, B. Wang, Z. Qin, J. Zhou, B. Lu, Electrochemical study of poly(2,6-anthraquinonyl sulfide) as cathode for alkali-metal-ion batteries, Adv. Energy Mater. 10 (2020), 2002780, https://doi.org/10.1002/aenm.202002780.
[16] S.G. Bratsch, Standard electrode potentials and temperature coefficients in water at 298.15K, J. Phys. Chem. Ref. Data 18 (1989) 1–21, https://doi.org/10.1063/1.555839.
[17] S.C. Kim, X. Kong, R.A. Vilá, W. Huang, Y. Chen, D.T. Boyle, Z. Yu, H. Wang, Z. Bao, J. Qin, Y. Cui, Potentiometric measurement to probe solvation energy and its correlation to lithium battery cyclability, J. Am. Chem. Soc. 143 (2021) 10301–10308, https://doi.org/10.1021/jacs.1c03868.
[18] F. Wang, J. Wang, G. Li, Z. Guo, J. Chu, X. Ai, Z. Song, A high-energy dual-ion battery based on chloride-inserted polyviologen cathode and LiCl/DMSO electrolyte, Energy Storage Mater. 50 (2022) 658–667, https://doi.org/10.1016/j.ensm.2022.05.055.
[19] O. Borodin, W. Behl, T.R. Jow, Oxidative stability and initial decomposition reactions of carbonate, sulfone, and alkyl phosphate-based electrolytes, J. Phys. Chem. C 117 (2013) 8661–8682, https://doi.org/10.1021/jp400527c.
[20] A.V. Marenich, J. Ho, M.L. Coote, C.J. Cramer, D.G. Truhlar, Computational electrochemistry: prediction of liquid-phase reduction potentials, Phys. Chem. Chem. Phys. 16 (2014) 15068–15106, https://doi.org/10.1039/c4cp01572j.
[21] N. Dardenne, X. Blase, G. Hautier, J.C. Charlier, G.M. Rignanese, *Ab initio* calculations of open-cell voltage in Li-ion organic radical batteries, J. Phys. Chem. C 119 (2015) 23373–23378, https://doi.org/10.1021/acs.jpcc.5b07886.
[22] S. Zhao, Z. Jin, J. Wu, New theoretical method for rapid prediction of solvation free energy in water, J. Phys. Chem. B 115 (2011) 6971–6975, https://doi.org/10.1021/jp201949k.
[23] M.J. Frisch, G.W. Trucks, H.B. Schlegel, G.E. Scuseria, M.A. Robb, J.R. Cheeseman, G. Scalmani, V. Barone, G.A. Petersson, H. Nakatsuji, X. Li, M. Caricato, A.V. Marenich, J. Bloino, B.G. Janesko, R. Gomperts, B. Mennucci, H.P. Hratchian, J.V. Ortiz, A.F. Izmaylov, J.L. Sonnenberg, D. Williams-Young, F. Ding, F. Lipparini, F. Egidi, J. Goings, B. Peng, A. Petrone, T. Henderson, D. Ranasinghe, V.G. Zakrzewski, J. Gao, N. Rega, G. Zheng W. Liang, M. Hada, M. Ehara, K. Toyota, R. Fukuda, J. Hasegawa, M. Ishida, T. Nakajima, Y. Honda, O. Kitao, H. Nakai, T. Vreven, K. Throssell, J.A. Montgomery, J.E. Peralta, F. Ogliaro, M.J. Bearpark, J.J. Heyd, E.N. Brothers, K.N. Kudin, V.N. Staroverov, T.A. Keith, R. Kobayashi, J. Normand, K. Raghavachari, A.P. Rendell, J.C. Burant, S.S. Iyengar, J. Tomasi, M. Cossi, J.M. Millam, M. Klene, C. Adamo, R. Cammi, J.W. Ochterski, R.L. Martin, K. Morokuma, O. Farkas, J.B. Foresman, D. J. Fox, Gaussian 16, Revision E.01, (2019).
[24] J.R. Pliego, J.M. Riveros, The cluster-continuum model for the calculation of the solvation free energy of ionic species, J. Phys. Chem. A 105 (2001) 7241–7247, https://doi.org/10.1021/jp004192w.
[25] D.G. Kwabi, V.S. Bryantsev, T.P. Batcho, D.M. Itkis, C.V. Thompson, Y. Shao-Horn, Experimental and computational analysis of the solvent-dependent O_2/Li^+-O_2^- redox couple: standard potentials, coupling strength, and implications for lithium–oxygen batteries, Angew. Chem. Int. Ed. 55 (2016) 3129–3134, https://doi.org/10.1002/anie.201509143.
[26] B. Zhang, J. Wu, S.Li J.Gu, T. Yan, X.P. Gao, The fundamental understanding of lithium polysulfides in ether-based electrolyte for lithium–sulfur batteries, ACS Energy Lett. 6 (2021) 537–546, https://doi.org/10.1021/acsenergylett.0c02527.
[27] T.A. Pham, K.E. Kweon, A. Samanta, V. Lordi, J.E. Pask, Solvation and dynamics of sodium and potassium in ethylene carbonate from *ab initio* molecular dynamics simulations, The J. Phys. Chem. C 121 (2017) 21913–21920, https://doi.org/10.1021/acs.jpcc.7b06457.
[28] M.D. Tissandier, K.A. Cowen, W.Y. Feng, E. Gundlach, M.H. Cohen, A.D. Earhart, J. V. Coe, The proton's absolute aqueous enthalpy and gibbs free energy of solvation from cluster-ion solvation data, J. Phys. Chem. A 102 (1998) 7787–7794, https://doi.org/10.1021/jp982638r.
[29] J. Li, Y. Hu, H. Xie, J. Peng, L. Fan, J. Zhou, B. Lu, Weak cation-solvent interactions in ether-based electrolytes stabilizing potassium-ion batteries, Angew. Chem. Int. Ed. 134 (2022), e202208291, https://doi.org/10.1002/anie.202208291.
[30] J. Holoubek, H. Liu, Z. Wu, Y. Yin, X. Xing, G. Cai, S. Yu, H. Zhou, T.A. Pascal, Z. Chen, P. Liu, Tailoring electrolyte solvation for Li metal batteries cycled at ultra-low temperature, Nat. Energy 6 (2021) 303–313, https://doi.org/10.1038/s41560-021-00783-z.